

LA-UR-23-30801

Accepted Manuscript

Spurious solar-wind effects on acceleration noise in LISA Pathfinder

Yang, Arnold
Desiderio-Sloane, Indie
Meadors, Grant David

Provided by the author(s) and the Los Alamos National Laboratory (1930-01-01).

To be published in: Classical and Quantum Gravity

DOI to publisher's version: 10.1088/1361-6382/adb538

Permalink to record:

<https://permalink.lanl.gov/object/view?what=info:lanl-repo/lareport/LA-UR-23-30801>



Los Alamos National Laboratory, an affirmative action/equal opportunity employer, is operated by Triad National Security, LLC for the National Nuclear Security Administration of U.S. Department of Energy under contract 89233218CNA000001. By approving this article, the publisher recognizes that the U.S. Government retains nonexclusive, royalty-free license to publish or reproduce the published form of this contribution, or to allow others to do so, for U.S. Government purposes. Los Alamos National Laboratory requests that the publisher identify this article as work performed under the auspices of the U.S. Department of Energy. Los Alamos National Laboratory strongly supports academic freedom and a researcher's right to publish; as an institution, however, the Laboratory does not endorse the viewpoint of a publication or guarantee its technical correctness.

PAPER • OPEN ACCESS

Spurious solar-wind effects on acceleration noise in LISA Pathfinder

To cite this article: Arnold Tianyi Yang *et al* 2025 *Class. Quantum Grav.* **42** 065024

View the [article online](#) for updates and enhancements.

You may also like

- [Advanced charge control dynamics simulation for the LISA gravitational reference sensor](#)
Samantha Parry Kenyon, Stephen Apple, John Siu et al.
- [Proceedings of the 5th International LISA Symposium and the 38th ESLAB Symposium, ESTEC, Noordwijk, The Netherlands, 12-15 July 2004](#)
Oliver Jennrich
- [Self-gravity modelling for LISA](#)
Stephen M Merkowitz, William B Haile, Shelly Conkey et al.

Spurious solar-wind effects on acceleration noise in LISA Pathfinder

Arnold Tianyi Yang^{1,2} , Indie Desiderio-Sloane^{1,3} 
and Grant David Meadors^{4,*} 

¹ Institute for Computing in Research, 145 Washington Ave, Santa Fe, NM 87501, United States of America

² Stanford University, 450 Jane Stanford Way, Stanford, CA 94305-2004, United States of America

³ California Institute of Technology, 1200 East California Boulevard, Pasadena, CA 91125, United States of America

⁴ Los Alamos National Laboratory, Los Alamos National Laboratory, PO Box 1663, Los Alamos, NM 87545, United States of America

E-mail: gdmeadors@lanl.gov

Received 31 July 2024; revised 7 February 2025

Accepted for publication 12 February 2025

Published 10 March 2025



CrossMark

Abstract

Spurious solar-wind effects are a potential noise source in future Laser Interferometer Space Antenna (LISA) measurements. One noise coupling mechanism is constrained by estimating solar-wind effects on acceleration noise in LISA Pathfinder (LPF). While LISA is designed for drag-free differential measurement, predicting the realistic impact both bounds the operational environment and assesses whether LISA could provide serendipitous space-weather observations. Data from NASA's Advanced Composition Explorer (ACE), situated at the L1 Lagrange point, serves as a reliable source of solar-wind data. The data sets are compared over the 114d time period from 1 March 2016 to 23 June 2016. This period gives the longest readily-available open data set, without interference from other commissioning activities. To evaluate space weather effects, the data from both satellites are formatted, gap-filled/interpolated, and fast-Fourier transformed for amplitude spectral density and coherence comparisons. Solar wind effects are not seen in a coherence plot between LPF and ACE; modest coherence in the planned LISA observational

* Author to whom any correspondence should be addressed.



Original Content from this work may be used under the terms of the [Creative Commons Attribution 4.0 licence](https://creativecommons.org/licenses/by/4.0/). Any further distribution of this work must maintain attribution to the author(s) and the title of the work, journal citation and DOI.

frequency band can be attributed to chance. This result indicates that measurable correlation due to solar-wind acceleration noise over 3 month timescales will be a negligible noise source. LISA is unlikely to inform solar wind measurements routinely. Another source of noise from the Sun, solar radiation pressure, is estimated to impart greater acceleration noise, but has yet to be analyzed.

Keywords: space weather, solar wind, gravitational waves, LISA

1. Introduction

The future Laser Interferometer Space Antenna (LISA) will be the first space-based gravitational wave detector on a heliocentric orbit [1]. The LISA mission expands upon the work of the ground-based Laser Interferometer Gravitational-wave Observatory (LIGO) [2], Virgo [3], KAGRA [4], GEO600 [5, 6], and their prototypes and partners, which have made significant contributions to our understanding of the Universe [7, 8]. LISA will measure frequencies ranging from approximately 0.1 to 100 mHz [1]. The LISA constellation will consist of three spacecraft in an equilateral triangle with arms 2.5 million km long, forming an antenna. This antenna will follow about 20 degrees behind the Earth. Each spacecraft will contain two centered, free-falling test masses. Deviations from the geodesic motion of the test masses are detected with time-delay interferometry (TDI) [1], using six laser links that connect each of the three spacecraft bidirectionally. TDI constructs a set of time series data, sampled every few seconds, from the combination of these laser links that represents that stretching of space, known as (dimensionless) strain. LISA's TDI output is, in effect, three virtual, correlated space-based interferometer channels, sensitive to gravitational waves with periods of seconds to minutes.

To confirm the viability of the LISA concept, the European Space Agency (ESA) developed and launched the LISA Pathfinder (LPF) [9, 10]. LPF consists of a test version of a LISA module—two free acceleration test masses held in the module's center. The LPF was launched on 3 December 2015, and traveled 1.5 million km from Earth to orbit the L1 Lagrange point; see figure 1 for positioning in relation to the Sun and Earth. The goal of LPF is to show that a drag-free control measurement technique is viable for a long-baseline gravitational-wave observatory.

By design, LISA will make differential measurements, with respect to 2 test masses per spacecraft, using TDI. LPF prototyped these 2 test masses, the second one located 38 cm from the first, to validate common noise-source rejection: solar radiation pressure, solar-wind, magnetic environment, and particle impacts. In addition, spacecraft acceleration was measured to observe external disturbances on a single-test mass signal. The *space weather* noise sources of solar wind (charged particles) and irradiance (photons), have been generally understood to be modest [11], below other factors, such as actuation fluctuations, Brownian noise, and external disturbances by micrometeoroids [12]. Test-mass charging may be affected by solar energetic particle (SEP) and galactic cosmic ray (GCR) flux [13], so space weather monitoring could provide forewarning. Index-of-refraction variations in plasma [14] may occur, related to the solar wind, but likely with less noise contribution than other sources [15]. While solar wind and irradiance are not dominant noise effects in LISA, they must be better understood for planning future space-based gravitational-wave observatories, including laser interferometers with even higher sensitivity—Big Bang Observer [16–18] and DeciHertz Gravitational-wave Observatory (DECIGO) [19, 20]—and atom interferometers, such as the Matter-wave Atomic Gradiometer Interferometric Sensor (MAGIS) [21]), a new technology applicable to

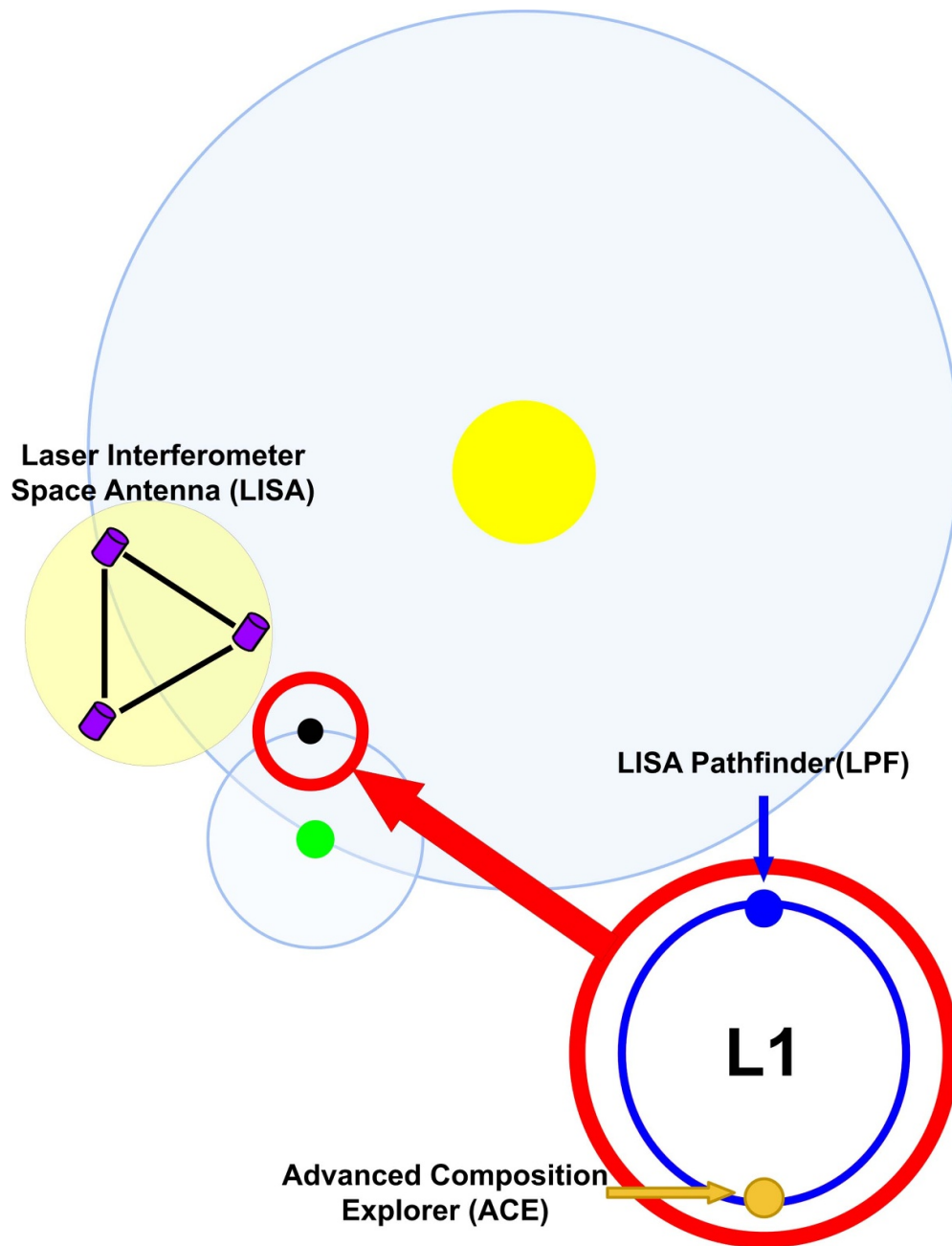


Figure 1. This diagram depicts the positioning of the LISA Pathfinder in relation to the Sun and Earth. The planned LISA system will be 20° behind the Earth.

space and not expected to use TDI. Another motivation, discussed momentarily, is the value of serendipitous space-weather indicators from LISA auxiliary measurements, such as acceleration. Theoretical extrapolation from solar wind and irradiance data to LISA [22] has set the stage for detailed analysis.

1.1. Related works

Space weather has been repeatedly identified as a noise factor in possible future LISA measurements [11, 13, 14, 22]. Past work that assessed space weather used SOHO's Virgo solar irradiance dataset [23–25] and the ACE solar-wind dataset to model possible impacts on the future LISA mission [22]. (For clarity, this paper will refer to the SOHO Virgo data simply as 'Virgo', as no data is used from the Virgo gravitational-wave observatory). Another major source of noise identified for LPF is micrometeoroids [12]. Through various models, 54 impact candidates were identified across a 4348-hour time period. They were shown to be similar to those resulting from Jupiter Family Comets (JFC), Oort cloud comets, Halley-type comets, and asteroids [12]. Additionally, the development of LISA is renewing the interest in the environment of space [14, 26, 27]. This environment includes SEP, GCR fluxes, and the effects of solar neutrons and interplanetary electrons [11].

Past theoretical extrapolations from ACE and Virgo data [22] have forecast low space-weather noise on LISA. The core task of the analysis here is to assess, using empirical comparison between LPF and ACE, whether these extrapolations are reasonably consistent with LPF experience. The small size of the field led to slow progress from the initial space-weather effect studies [11, 13] to plasma refraction [14] and to the study of ACE and Virgo [22], which focused on forward modeling. A comparison of in-situ acceleration data with the solar wind is needed.

1.2. Motivation

This manuscript considers whether correlations are measurable between solar wind and LPF acceleration data. Analyzing LPF's data can be proof that solar-wind noise impact is minimal or demonstrate that in the future, LISA might act as a serendipitous solar-wind sensor at an unusual orbit, an idea originally presented in the 2000s [11]. Similar to STEREO [28], it might provide measurements near 1 AU, along Earth's orbit, but at a different orbital phase and position along the Schatten Current Sheet. Unlike STEREO, LISA would not move significantly with respect to Earth over the nominal 4-year mission duration. While numerous spacecraft collect space weather data, such as the Solar and Heliospheric Observatory (SOHO) [23–25], Wind [29] and DSCOVR [30] at L1, the Ulysses mission at high ecliptic latitude [31], and the Parker Solar Probe [32, 33] and Solar Orbiter [34] near the Sun, a long-lasting observation point off the Earth–Sun line-of-sight, thus a different Carrington longitude, could constrain space-weather models to the benefit of future forecasts. Measuring space-weather model skill scores [35] and comparing to observation [36] is routine, and LISA could afford a comparison at a unique vantage point.

Observing space weather is not the primary goal of LISA. While coupling into the gravitational-wave TDI channels would negatively impact astrophysics, TDI by construction should allow first-order cancellation of spacecraft acceleration, so measurable accelerations could conceivably occur simultaneously with LISA astrophysics. Conversely, if accelerations match the predictions of space-weather models at LISA's orbital position, then those predictions might be used as a feedforward signal to cancel a fraction of the acceleration.

The Drag-Free Control and Attitude Systems (DFACS) [37] on LISA and LPF should (independent of TDI) reject any spurious acceleration in principle, warranting a clarification. The DFACS preserves the residual differential acceleration between the test masses from external disturbances, to within a noise budget, in 15 degrees of freedom (DOF), including 6 drag-free DOF. The design of the LISA DFACS is active and ongoing following LPF [38, 39] and has already adapted to consider the aforementioned micrometeoroid impacts [40]. During LPF,

DFACS performance was better than requirements for the noise budget, and in failure conditions, its Fault Detection, Isolation, and Recovery systems behaved as expected, assuring safe return to science operation [41]. Because solar-force acceleration is already accounted in the noise budget, being well below the total spectral noise, the motivation for searching for this effect requires restatement. In addition to curiosity from the viewpoint of serendipitous space-weather observations, the DFACS (on the LPF as-flown design) uses solar pressure as a virtual thruster, due to the permanent sunward orientation of the z -axes. The pressure provides virtual actuation authority in the negative z -direction [41]: all cold-gas thrusters are canted in the same negative- z direction, thus providing thrust only in the positive z -direction. It is important for any scheme using solar forces for virtual actuation to have characterized the variability in those forces, which this manuscript intends to help to do. Moreover, actuation crosstalk [41] between axes involving the cold-gas/solar-force micro-propulsion system might conceivably lead to variability in these forces affecting other control axes. While DFACS has comprehensively managed these effects to date, this study aims to scope the full range of possible issues with solar-force acceleration.

Acceleration can come both from sunlight and solar wind. Sunlight itself will exert solar radiation pressure on the spacecraft, linearly proportional to the solar irradiance. Although this effect is expected to be about 10-fold larger than the solar wind [22], it is more complicated to model the varying spacecraft reflectivity and albedo, so this paper focuses on solar wind as a proof of principle.

Constant solar wind, sunlight radiation pressure, or other static forces are not expected to have a direct impact on LISA gravitational-wave measurements, though small accelerations might have a long-term impact on LISA's orbit. A time-varying force could also perturb operations, particularly if the three spacecraft experience the differential forces due to orbital position and orientation. Studies of solar wind variability [42] demonstrate that the solar wind can vary from 350 to 700 km·s⁻¹ in the span of a week, doubling the solar-wind force on a timescale of less than 10⁶ s, motivating an investigation of μ Hz to mHz frequencies, even though they are below the typical LISA science band. The idea was tested by comparing the LPF spacecraft's z - and x - axis data with the corresponding advanced composition explorer (ACE) solar-wind data from 1 March 2016, to 23 June 2016 [43]. The solar wind electron proton alpha monitor data is used. ACE [44] orbits L1, like LPF; SOHO and DSCOVR might provide similar data, but ACE is well-sampled over LPF's mission and can be readily compared with prior literature [22]. This data can be modeled and compared with the data from LPF to analyze the effects of solar wind.

1.3. Limitations

This 114 d duration is a severe limitation on the scope of the study, but it is the longest readily-available open data set, based on the recommendations of the LPF team that analyzed micro-meteoroid impact [12], because other intervals were affected by interference from commissioning activities. LPF launched after solar maximum, lasting 576 d, so performance across the entire solar cycle is yet unknown. Though Fourier-domain, sinusoidal-injection validated methods used in this analysis do provide a complete basis set for finding direct, linear couplings at the measured timescales, nonlinear 'upconversion' of solar-wind noise to higher frequencies cannot be ruled out. Future studies of *higher-order spectra* (such as bispectral analysis) [45] could probe nonlinear couplings. Because such effects can arise from couplings between spacecraft components, it is challenging to simulate and realistically validate these methods even with more complex waveforms; this manuscript is restricted to the linear case.

As LPF is no longer operational, data from LISA itself will be needed to provide more data and characterize spacecraft interactions.

2. Methods

Data from ACE and LPF are obtained from NASA and are re-distributed [46, 47]. The source code for the analyses, primarily written in Python, is also linked in the supplementary data. This code is used for filtering, normalization, coherence, and plotting.

The coordinate axes differ between LPF and ACE. For LPF, the z -axis refers to the vector normal from the LPF spacecraft body *top deck* [12, 48]. Crucially, this convention differs from past theoretical studies about LISA [22], but it is consistent with the data files linked in the Supplementary Data. The z -axis is typically kept within 2 degrees of radial toward the Sun: it would see the majority of any solar-wind effect. The x -axis is defined as pointing from Test Mass 1 to Test Mass 2. Usually perpendicular, the x -axis might be tilted toward the Sun up to the 2-degree limit noted above. LPF was not tilted in the y -axis, which is defined by the right-hand rule to complete the coordinate system between x and z . Because of this orientation, no coupling is expected between radial solar wind and the y -axis.

Conversely, the ACE data, listed in Supplementary Data, uses the Geocentric Solar Ecliptic (GSE) GSE coordinate system [49]. In this system, the Earth–Sun line defines the x -axis, and the z -axis is defined by the ecliptic north pole; the y -axis is defined implicitly by the right-hand-rule. The ACE x -axis is therefore, up to a sign and the aforementioned 2-degree uncertainty, parallel to the z -axis for LPF. In the Fourier analysis that we perform, any sign flip amounts to a π phase shift, which does not affect the magnitude of the spectrum nor the coherence plot. In the ACE data set, the outgoing solar wind has a minus sign, but we do not consider the sign further.

Figure 2 shows the steps to plot and compare the ACE and LPF data sets. We first format both data sets to include only data present within the time frame and for the axes being studied. Next, we filter and gap-fill the ACE data set because the data set is in time-series format. An Inverse Fast Fourier Transform (IFFT) is applied to the LPF data set because the set is in the frequency domain [50]. Once the IFFT is performed, the LPF data is filtered and gap-filled. The ACE data set must be modeled onto LPF. Lastly, both data sets are plotted and compared.

2.1. Process for Creating Plottable ACE Data

Solar-wind data is obtained from the ACE. ACE data includes information on solar-wind velocity components (x, y, z), α -particle to proton ratios, proton densities, and proton speeds at 64 s intervals measured in Coordinated universal Time (UTC) [43]. The area of the solar array is modeled as a 2.9 m diameter flat circular array, based off of the concept spacecraft design [1]. This total area is only used in the LPF solar-wind force calculations, so a flat-circular assumption, consistent with the spacecraft design, is presumed sufficient. A more sophisticated study might take into account the different spacecraft facets, and for solar radiation pressure, albedo would be relevant. Based on the published spacecraft design, we speculate that the ‘model uncertainty’ between the true, approximately-cylindrical spacecraft and the flat-circular array assumption is less than the uncertainty in other measurements.

ACE’s UTC measurements are converted to GPS time, because the LPF data is in GPS time. Bad data values from the ACE data are also removed (the ACE data header specifies that bad data is indicated by the value -9999.9) [43]. The gaps created by removing the bad data are

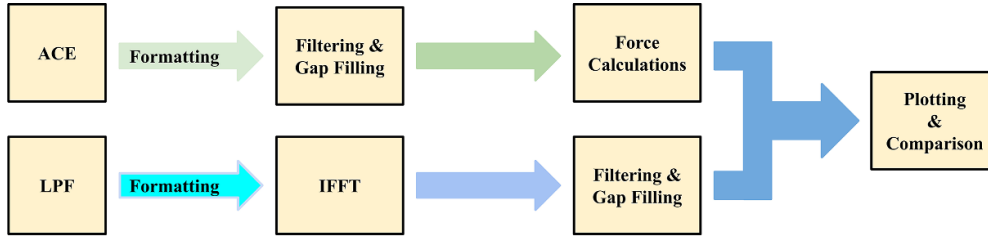


Figure 2. Steps undertaken to reach two comparable data sets: both datasets are converted into a readable format, and ACE’s time frame is trimmed to match LPF. LPF data is stored in the frequency domain, so an inverse FFT is performed before filling in missing data blocks. ACE data is in time-series format, bad data (as indicated by code specified in the data header) is replaced, then ACE data is modeled onto LPF through force calculations, equations (7)–(9).

Table 1. Gap-fill methods by gap length. This set of methods is adapted from a previous publication [22]. Further details are elaborated in section 2.1. Gap lengths are measured in data indices for either ACE or LPF data.

Type	Length of gap	Fill method
A	1	Linear interpolation
B	2–24	Gaussian noise with linear Interpolation
C	≥ 25	Tukey window (Half-Hann Window, taper to 0)

split into three categories based on the process described in *Modeling Spurious Forces on the LISA Spacecraft Across a Full Solar Cycle*[22].

Type A gaps are missing one data point and are filled using linear interpolation.

Type B gaps are missing two to twenty-four data points and are filled using linear interpolation with Gaussian noise. Equation (1) defines Gaussian noise (σ) where σ_1 and σ_2 are the standard deviations found by sampling data of equal length to the gap on either side of the ACE data gap. In the equation, for the i th entry in a gap of length l such that $1 \leq i \leq l$, a point is generated based on σ_1 and σ_2 [22].

$$\sigma = \frac{l - (i - 1)}{l + 1} \sigma_1 + \frac{i}{l + 1} \sigma_2 \quad (1)$$

Type C gaps are missing twenty-five or more data points; they are filled using half a Hann window (sometimes incorrectly known as ‘Hanning’ [51]) with a slow fall-off to zero, as defined by equation (2) [22]. This is also known as a *Tukey* window [51]. Twenty-five data points on either side of the gap are used to calculate simulated interpolation data $\omega(n)$ where $N = 51$ and $0 < n < N - 1$, creating the data to fill a Type C gap.

$$\omega(n) = 0.5 \left[1 - \cos \left(\frac{2\pi n}{N - 1} \right) \right] \quad (2)$$

As noted in the literature [22, 51], windowing (Hann/Tukey) mitigates Gibbs phenomena due to discontinuities in the time series, which can introduce side lobes in the frequency domain. Different windowing methods modify the spectrum of side lobes; without an explicit window function, the implicit windowing induced by a finite sample duration imparts a *de facto* rectangular window, with more severe side-lobe distortion than a window such as

the Hann or Tukey. This distortion is exacerbated by multiple discontinuous data segments. The explicit Type C gap method, with windowing, suppresses these side lobes, enhancing the analysis. Coherence measurements might be affected by windowing choice if spectral peaks were orders of magnitude above background, a situation not seen in this data set, making the choice of Type C method robust. In principle, more sophisticated methods, such as Gaussian Processes, could be used, as done for past work on Virgo [22], due to its more complicated gap distribution. As past work has used the Hann/Tukey method on ACE, and additional validation would be required for Gaussian Processes, we use the Hann/Tukey method here for ease of comparison and implementation.

Following previous methods [22], the force exerted on the satellite by solar-wind particles is calculated using ACE data. Equation 3 calculates the number of protons (N_p) and α -particles (N_α) hitting the satellite per unit of time,

$$N = nvA \cos(\phi) \quad (3)$$

with n being particle density and v being wind speed. The surface area of the LPF solar array is represented by A . R is the fraction of particles reflected. ϕ represents the angle between the normal of the array and the orbital plane [22]. LPF's η sensor data of the second test mass showed that ϕ was less than $\pm 1 \times 10^{-7}$ for all values, making it reasonable to assume ϕ in that case to be 0. The η sensor data is stated to be within a 2-degree margin of error. Therefore, both a 0-degree and 2-degree value for the angle are tested. Equations 4, 5, and 6 are used to calculate the final forces for the x and z axes. The y -axis equation was disregarded as the amount of force occurring on that axis was negligible [22].

The following equations are reproduced verbatim from previous LISA analysis [22]:

$$F_x = (N_p m_p + N_\alpha m_\alpha) [(1 + R \cos(2\phi)) v_x + R \sin(2\phi) v_z], \quad (4)$$

$$F_y = (N_p m_p + N_\alpha m_\alpha) [(1 - R) v_y], \quad (5)$$

$$F_z = (N_p m_p + N_\alpha m_\alpha) [(1 + R \cos(2\phi)) v_z + R \sin(2\phi) v_x] \quad (6)$$

N_p , the proton collision rate, and N_α , the α -particle collision rate, were found using equation 3. The proton and α -particle masses from the ACE solar-wind data are represented by m_p and m_α . The x , y , and z components of solar-wind velocity are represented by v_x , v_y , and v_z . Assuming the worst-case scenario (that all the particles reflect), R will be defined as 1. Then equations (4)–(6) can be simplified to the following [22]:

$$F_x = (N_p m_p + N_\alpha m_\alpha) [(1 + \cos(2\phi)) v_x + \sin(2\phi) v_z], \quad (7)$$

$$F_y = 0, \quad (8)$$

$$F_z = (N_p m_p + N_\alpha m_\alpha) [(1 + \cos(2\phi)) v_z + \sin(2\phi) v_x]. \quad (9)$$

The ACE solar-wind force values derived using equations (7)–(9) are now able to be compared to the processed LPF data by being plotted and transformed as described in section 3, for figures 3 and 4. For figure 5 onwards, an additional step is taken, upsampling ACE data from its 64 s cadence to the 2.5 s cadence of LPF with interpolation. This step aligns ACE data with LPF to allow coherence measurements, with the caveat that information above ACE's Nyquist frequency (7.8125 mHz) may be aliased and should be treated with caution.

2.2. Process for Creating Plottable LPF Data

Data from the LPF is used to predict the effect of solar-wind on the future LISA data. The LPF data obtained from the NASA Goddard Space Flight Center combines information from various sensors to estimate the free-body motion of LPF. The data spans 114 d and is organized into 370 files, each 16384 s long. The data is at 2.5 s intervals from the second sensor on the x -axis and the second sensor on the z -axis. The data for LPF is in the frequency domain; thus, an IFFT was applied. The IFFT adds the complex conjugates of negative values and zeros to the positive, non-zero values, returning the data to the original time series format. To calculate force, the acceleration from the IFFT is multiplied by the mass, 422 kg [52]. The 31 gaps in both the x and z axes are filled using the Tukey Window (Type C) method (table 1) [22].

2.3. Plotting methods

A native sample-rate time-domain comparison and a Fourier transform comparison are used in figures 3 and 4, respectively, to check for large-scale similarities between the spacecraft. The time domain data is zero-meant to highlight the differences in the force data collected between LPF and ACE. Zero-meaning removes any constant component to the force data, although overall trends and periodic variation are preserved. The zero mean was chosen to aid Fourier-transform normalization; in the frequency domain, the mean is equivalent to the zeroth frequency bin, encompassing oscillations slower than the 114 d period, which we do not consider in any case. The `scipy.signal.coherence()` function is used to determine magnitude-squared coherence between LPF and ACE data and the averages of different lengths of correlation values [53], using Welch's method. As noted in figures 5–8, ACE data is upsampled, and those coherence comparisons use increasing segment lengths, multiplying by factors of 4 from 1 to 4^5 .

3. Results

Figure 3 depicts a time series that presents a direct comparison between the LPF time domain and the ACE force time domain, with both datasets zero-meant. The ACE force data is calculated using the force equations and a 2-degree estimate for LPF angle ϕ . The time series do not show any large, visually-evident correlation between ACE and LISA data. Long, constant segments in LPF indicate data gaps.

Figure 4, using the time-series data from figure 3 as input, presents an amplitude spectral density (ASD) of ACE and LPF data. Nothing is significant enough to be seen as a solid correlation between the two data sets. An FFT is done with a $1/N$ normalization coefficient and a sampling time interval of $dt = 2.5$ s and $dt = 64$ s for LPF z -axis and ACE x -axis force data, respectively. A spectral peak that appears at about 3 mHz, near the 5 min solar oscillation [54] is spurious on closer inspection, because it is not found at the same frequency in both spacecraft. No other peaks appear coincident nor overlapping. The small ratio of ACE-inferred to LPF-measured force indicates that no more than a few percent of LPF acceleration motion is directly attributable to the solar wind.

Coherence plots can measure correlations as a frequency-domain spectrum, dimensionless, normalized to be between zero and unity. From the coherence plot (figure 5), it is observed that the coherence between the two data sets is minimal, and any correlation is probably due to random chance. In particular, spectral lines in LPF do not show coherence with ACE on closer inspection, and are therefore believed to be instrumental artifacts.

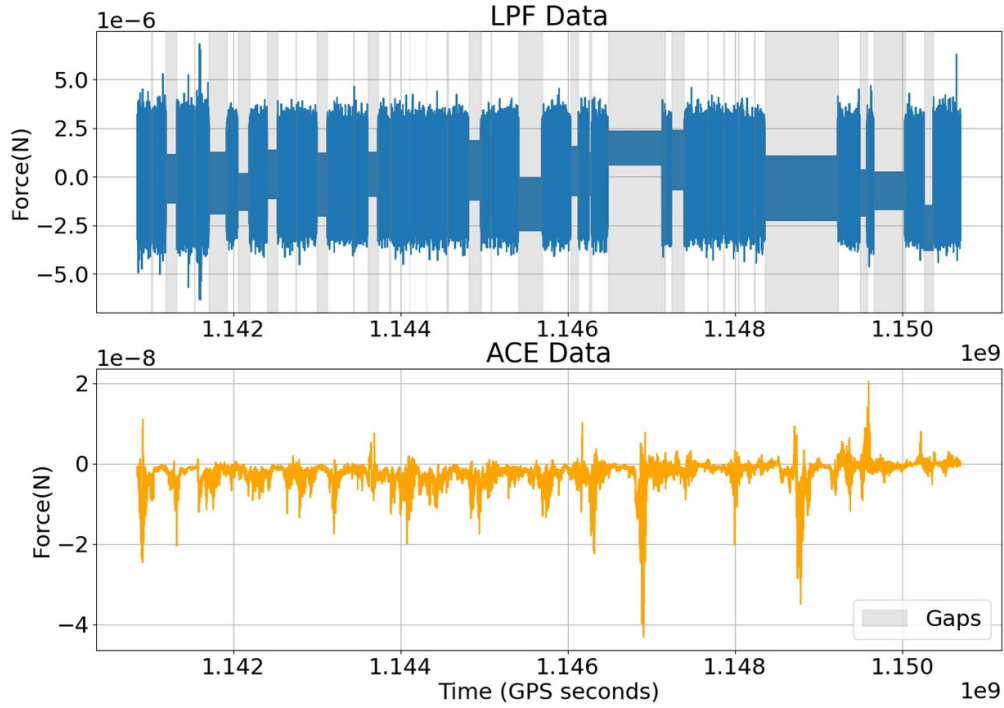


Figure 3. Time-domain plot of data for the LPF z -axis and the ACE x -axis, which are parallel to the Earth–Sun line. Data is zero-meaned, and a 2-degree tilt estimate (from z toward x) is used for the ACE’s force model, coupling solar-wind velocity to imputed acceleration on LPF. Although the solar wind only is expected to push outward on ACE, zero-meaning can result in the appearance of a negative-sign force. ACE, as an operational satellite, has gaps filled as in section 3.1, but they are not of comparable length to LPF. A total of 31 gaps in the LPF data are filled per section 2.2. LPF gaps of discernible length in this figure are shaded for clarity; some gaps may be too short to render. These gaps largely arise from LPF operations and commissioning periods.

As with power-spectral density, coherence measurements follow noise statistics: a value in the coherence spectrum is significant only if it is a peak above the background. Averaging improves the noise statistics by subdividing the data, at the cost of eliminating sensitivity to slow (long duration) effects. With magnitude-squared coherence (to which the term *coherence* used through this paper always refers), the noise floor typically is inversely linearly proportional to the number of averages, N . To balance this tradeoff, N is illustrated across several values. Low N is displayed to check for any possible low-frequency correlation, and increased N allows a higher-sensitivity check for high-frequency correlation.

Figure 5 shows three different lengths of coherence value averages for the ACE x -axis and LPF z -axis. Each decrease in the values averaged increases the accuracy of the line. As the accuracy increases, the coherence noise floor decreases. The low coherence indicates that solar-wind will have little to no direct affect on the future LISA. Specifically, the $N = 4$ coherence spectrum constrains any magnitude-squared coherence above about 0.1 down to the cutoff at the lowest frequency bin, $1 \mu\text{Hz}$, or conservatively at least above $10 \mu\text{Hz}$. The $N = 64$ spectrum is about a factor of 16 lower, and the $N = 1024$ spectrum another 16-fold lower, with typical

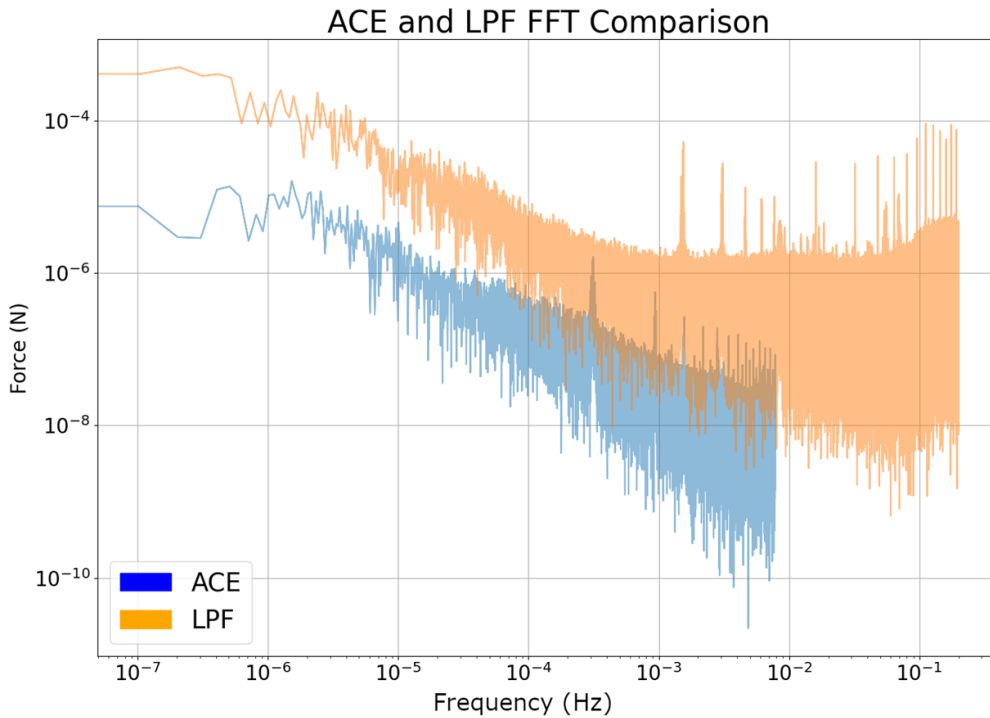


Figure 4. Force amplitude spectral density (ASD) using the Fourier-transform of the ACE and LPF force time series from figure 3. The spectra show the ACE x -axis and LPF z -axis, which are parallel to the Earth–Sun line. Despite the presence of spectral lines in both ACE and LPF, such as a spectral line near a 5 min oscillation period in helioseismology [54], on closer inspection no coherent features are shown between the two spacecraft. The spectral densities are computed using the native time resolution of the data.

values no higher than 10^{-4} down to the minimum frequency of about 1 mHz, or conservatively at least above 10 mHz. A correlated force between ACE and LPF should generate a coherence peak that would be, if above the minimum frequency, consistent in height with increasing numbers of averages. No such peak is found.

Figure 6 illustrates the same principle for the ACE z - and LPF z -axes. It is possible for the LPF x -axis to have up to 2 degree tilt toward the Sun, allowing about 7 percent of the force of the face-on solar wind to accelerate the spacecraft in the x -direction, while the decrease in the z -direction would be less than 2.5 percent. Moreover, ACE’s z -axis is orthogonal to the solar wind axis, so solar wind in that direction is typically one to two orders of magnitude less than in the ACE x -axis, and its variation is not consistently correlated with overall solar-wind speed. The net result is that the ACE z - and LPF z -axes should be close to a null experiment, with much less correlation than the ACE x - and LPF z -axes. If a correlation were seen in the latter, then figure 6 could provide a realistic picture of the coherence-spectrum background. In the present situation, figures 5 and 6 are very similar, and no correlation is evident in either plot.

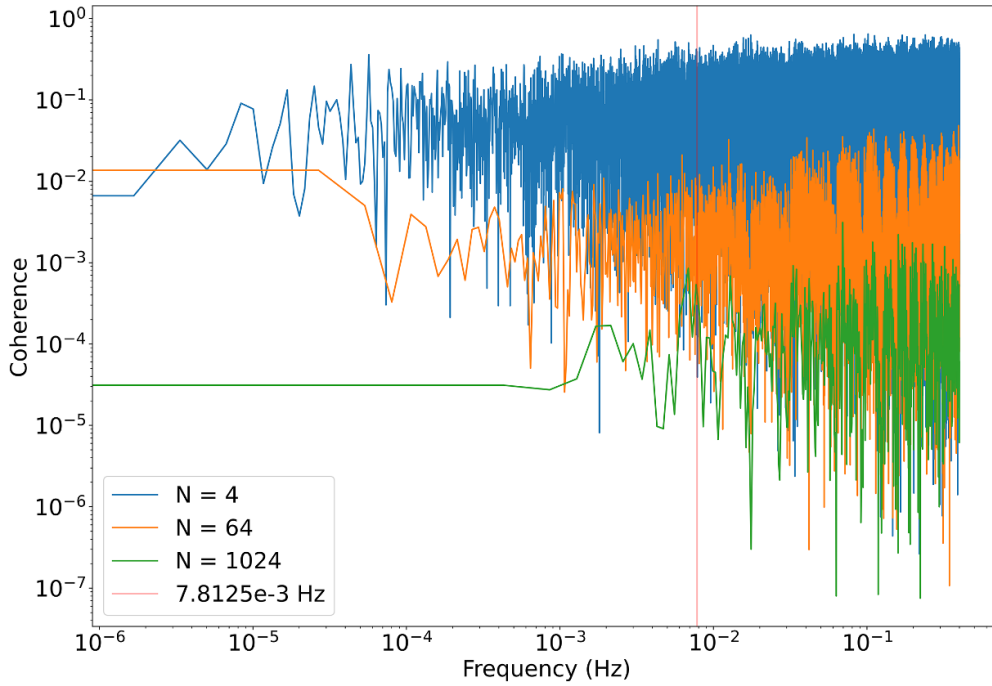


Figure 5. Magnitude-squared coherence (frequency-domain correlation) between ACE and LPF data sets through three different lengths of coherence value averages. (Three more lengths were tested but omitted for clarity). The coherence is between the ACE x -axis and LPF z -axis, which are parallel to each other and the Earth–Sun line. A 0-degree tilt estimate was used for the force model converting ACE solar-wind to LPF force; the difference between a 2-degree estimate and the full face-on solar wind force is less than 0.3 percent. N is the number of coherence averages used. To compute the coherence, ACE data (64 s time resolution) was upsampled to LPF’s cadence (2.5 s time resolution), so a vertical line has been marked at 7.8125×10^{-3} Hz, the native ACE Nyquist frequency. Coherence length is varied for two reasons. First, low N was used to detect any possible low-frequency correlation. Second, increased N shows decreasing coherence, constraining any possible high-frequency correlation. Per a visual estimate from the spectrum, low levels of low-frequency magnitude-squared coherence, below about 0.1 at $10 \mu\text{Hz}$ or 10^{-4} at 10mHz , cannot be conclusively ruled out without longer-duration data, but no evidence of physical correlation is apparent.

4. Test verification

To ensure the accuracy of the previous results and to create a simulation of a distinct signal, the correlation methods are tested with simulated data. The ACE z and LPF z axes are used to provide data that have realistic noise but presumed-minimal, currently-undetectable coupling. A measured, known sinusoidal excitation is added (‘injected’) to both the LPF and ACE real, time-series data sets after they are filtered, gap-filled, and post-processed. The force time series follows $F(t)$:

$$F(t) = A \sin(2\pi ft + \phi) \quad (10)$$

In equation (10), $F(t)$ represents the *force* excitation added to the data, where A is amplitude, f is frequency, t is time, and ϕ is phase. The phase is set to 0, because it does not affect the

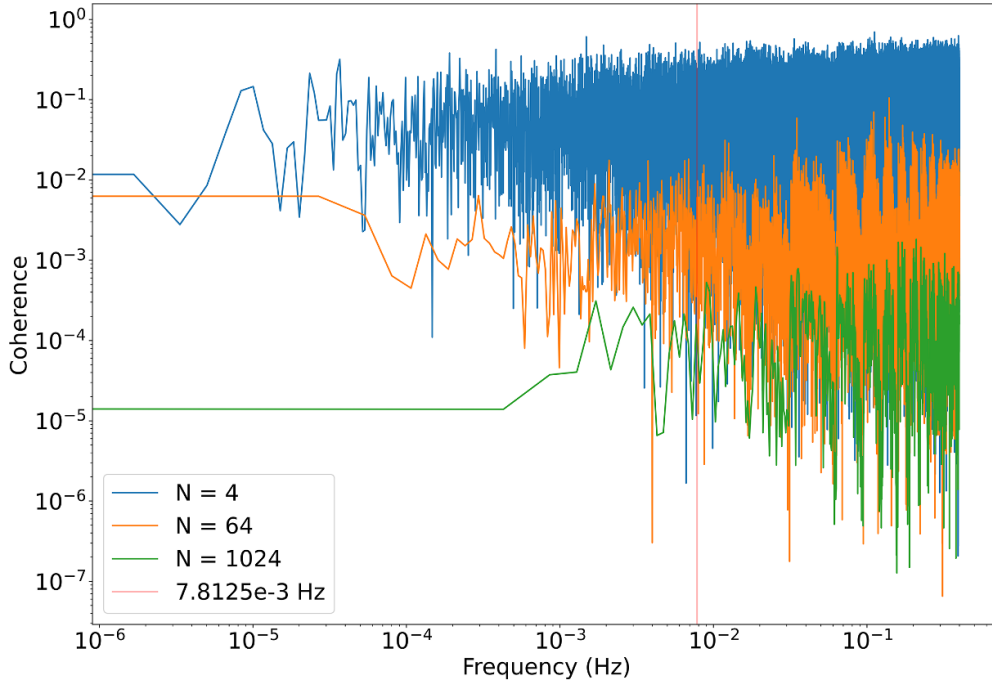


Figure 6. Magnitude-squared coherence (frequency-domain correlation) between ACE and LPF data sets through three different lengths of coherence value. (Three more lengths were tested but omitted for clarity). The coherence is between the ACE z -axis, which is oriented toward the ecliptic north pole and the near-orthogonal LPF z -axis, which is parallel to the Earth–Sun line. To compute the coherence, ACE data (64-s time resolution) was upsampled to LPF’s cadence (2.5 s time resolution), so a vertical line has been marked at 7.8125×10^{-3} Hz, the native ACE Nyquist frequency. A 2-degree tilt estimate was used for the ACE force model, to test for a hypothetical coupling of about 7 percent of face-off solar wind force between the otherwise-perpendicular x -axis to forces along the Sun-ward radial direction. N is the number of coherence averages used. Per a visual estimate from the spectrum, as with figure 5, no evidence of physical correlation is apparent.

coherence measurement. Amplitude and frequency are varied as follows. Adding this excitation in both sets of data simulates a specific frequency of the wave that should then be picked up by the coherence function, thus showing an excitation in that frequency on the coherence plot.

Different force levels are tested separately. The force F is the force amplitude at a specific frequency, which differs from the force value in an ASD bin. Values of 0.2 nN and 5 nN cover the low and high range of *detectability* in this study, although both are much higher than typical of solar-wind force in the LISA band. Such large forces are needed to be detectable at all, and realistic forces (below or at 20 pN, seen at the year 2000 maximum [22]) will have less coherence.

In each test, a single sinusoidal frequency is excited. Multiple frequencies are excited across independent tests. The test frequencies 1×10^{-4} Hz, 5×10^{-4} Hz, 1×10^{-3} Hz, 2×10^{-3} Hz, 5×10^{-3} Hz, and 1×10^{-2} Hz are measured. All frequencies display distinct excitation at the injected frequency in the coherence spectrum. The tests also vary in force, for the least

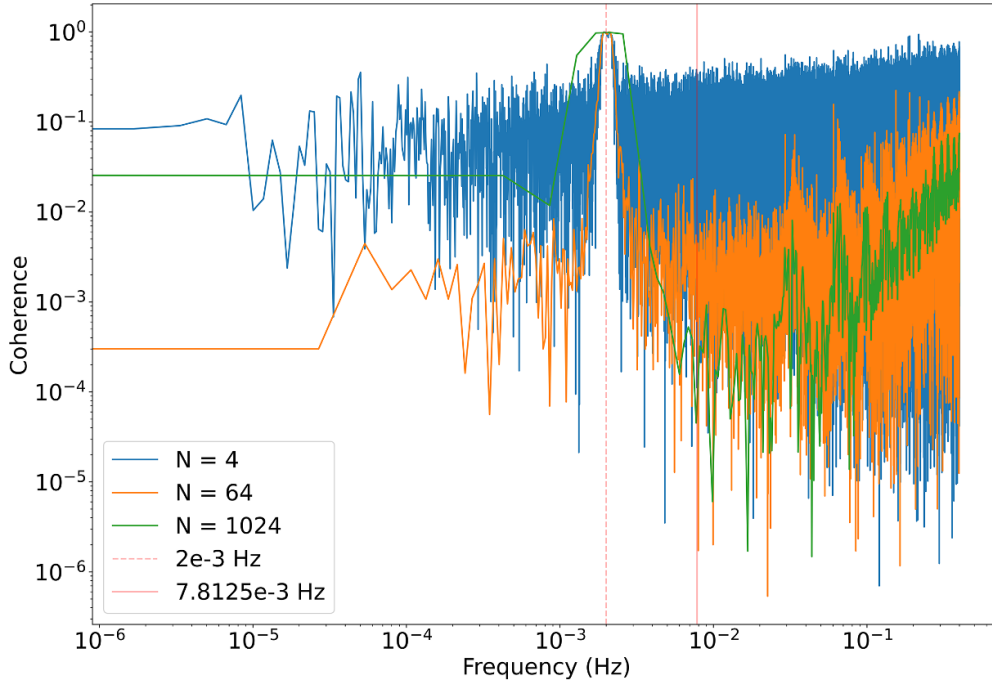


Figure 7. Magnitude-squared coherence test of data with simulated frequency at 2×10^{-3} Hz and amplitude of 5 nN. N is the number of segments for coherence used. At 1024 points per segment, there is 99.54% correlation. A vertical line has been marked at 7.8125×10^{-3} Hz, the native ACE Nyquist frequency; ACE data is otherwise upsampled to match the LPF sampling rate. This simulation is injected into time-series force data from the ACE z -axis and the LPF z -axis, which are physically near-orthogonal and do not display visible correlation in figure 6.

excitation needed for at least 50% correlation, when 1024 points are used per segment. To illustrate this, figure 7 shows the frequency 2×10^{-3} Hz at 99.5% coherence for 1024 segments per average with 5 nN force, and figure 8 shows the frequency 5×10^{-3} Hz at 68.36% coherence for 1024 segments per average with only 0.2 nN force. Figure 9 shows the frequency 5×10^{-3} Hz again, but with the same 5 nN force as figure 7, displaying a similar 99.9% correlation, thus showing that the coherence function works accurately for comparing ACE and LPF datasets.

The excitation frequencies of 2 and 5 mHz in this paper's figures 7–9 represent the low-to-mid range of LISA, relevant to both the galactic white-dwarf binary population and black-hole mergers around a million solar masses. At these frequencies, prior work [22] has estimated the force coupling of solar wind pressure into LISA: figure 3 of that paper shows forces in the year 2000, near solar maximum, resulting in a predicted force at 2 mHz of roughly 20 pN, and less at 5 mHz. While a comprehensive statistical sampling from that work's force spectrum is reserved for future research, this paper shows that near 200 pN (0.2 nN), magnitude-squared coherence levels do reach above 0.68, or about two-thirds, at 5 mHz. Comparing the two values, the coherence would be expected to be lower at 2 mHz, consistent with the rise in ACE and

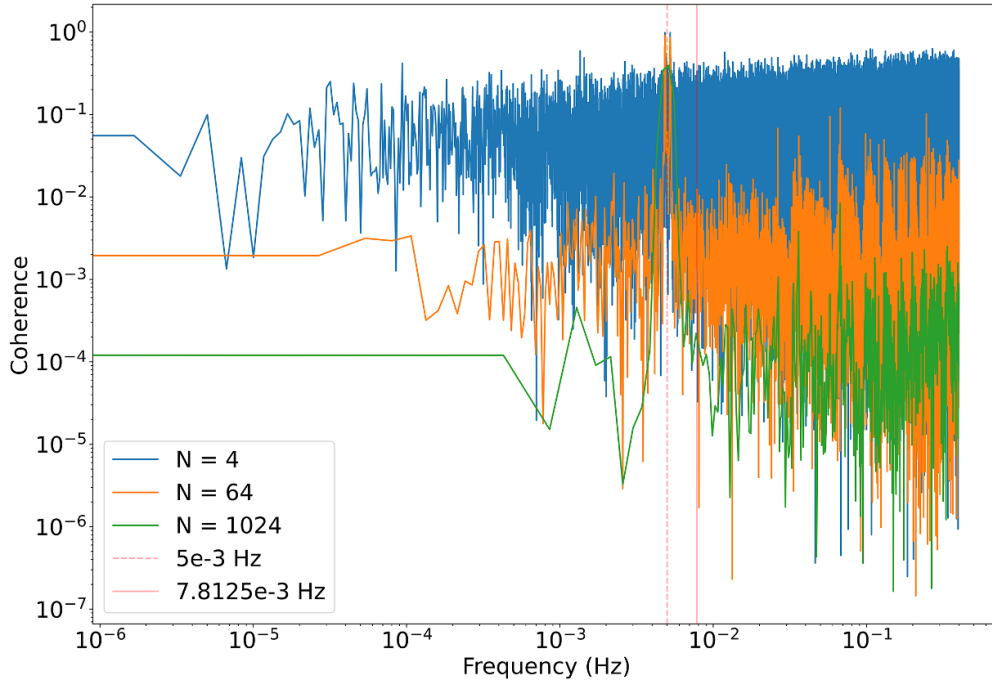


Figure 8. Magnitude-squared coherence test of data with simulated frequency at 5×10^{-3} Hz and amplitude of 0.2 nN. N is the number of segments for coherence used. At 1024 points per coherence segment, there is 68.36% correlation. A vertical line has been marked at 7.8125×10^{-3} Hz, the native ACE Nyquist frequency; ACE data is otherwise upsampled to match the LPF sampling rate. This simulation is injected into time-series force data from the ACE z -axis and the LPF z -axis, which are physically near-orthogonal and do not display visible correlation in figure 6.

LPF noise spectra toward lower frequencies. These results affirm, with empirical data, prior statements that the solar wind should not be a significant noise source for LISA.

5. Conclusion

The proposed spurious effects of ACE x -axis measured solar wind on acceleration noise of LPF data from the z -axis are thoroughly analyzed. As shown in figures 5 and 6, the coherence between the ACE and LPF data is sporadic for the given frequency range: average correlation for each data section was of order 0.1 or less. Coherence tests verify that there is a measurable correlation for a simulated excitation of known amplitude, as seen in figures 7–9. The analysis shows that any correlation seen in available real, unexcited data is indistinguishable from a chance relationship. The force models for the x - and z -axes found a negligible relation between the ACE solar wind and LPF acceleration data.

While direct solar-wind acceleration noise have not been anticipated in the literature to contribute significantly to LISA’s noise budget, this study corroborates this belief with empirical data. Caution is warranted, as solar radiation pressure, another noise factor with likely greater effects on LPF, has yet to be tested [22], and the limited 3-month time frame of data that were analyzed means that correlations over longer timescales are possible. More detailed analysis

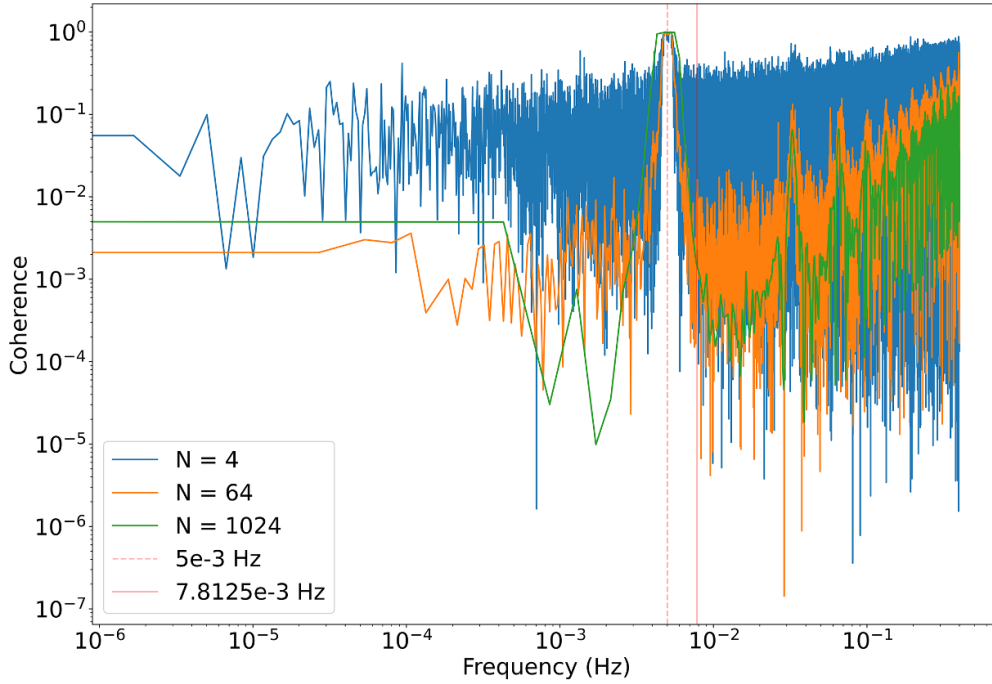


Figure 9. Magnitude-squared coherence test of data with simulated frequency at 5×10^{-3} Hz and amplitude of 5 nN. N is the number of segments for coherence used. At 1024 points per coherence segment, there is 99.9% correlation. A vertical line has been marked at 7.8125×10^{-3} Hz, the native ACE Nyquist frequency; ACE data is otherwise upsampled to match the LPF sampling rate. This simulation is injected into time-series force data from the ACE z -axis and the LPF z -axis, which are physically near-orthogonal and do not display visible correlation in figure 6.

is warranted, as solar variability could reach levels even higher than in 2000; the 2015 to 2017 LPF operation period was of short duration and after solar maximum, albeit before solar minimum. Conversely, solar wind may vary inversely with particle density, and irradiance varies separately, so the total dynamic pressure may not consistently vary with wind speed or the phase of the solar cycle. Connections with the space weather community can help to contextualize the limited available data.

Future analyses could also focus on working with individual subsets of the data and plotting the relationships between those to eliminate the possible confounding effects created when using gap-fill methods. More detailed models of spacecraft charging for the solar wind, as well as albedo for solar radiation pressure forces, could improve model fidelity. Higher-order spectra could identify nonlinear couplings, with value enhanced by detailed understanding of spacecraft interactions. Further study might reveal issues that, while not of consequence to LISA operation or design, inform BBO, DECIGO, MAGIS, or other proposed space-based gravitational-wave observatories, using laser or atom interferometry or still other techniques.

These findings are encouraging for the future of space-based laser interferometry: there is a reasonable safety margin between solar wind forces and measurable acceleration noise in LPF, and by extension, LISA. To the benefit of gravitational-wave astronomy, though not the

space weather community, it currently appears difficult, with such low coherence at expected force levels, to solve the inverse problem of finding solar wind force from LISA acceleration, as proposed previously [11]. Space weather noise should not unexpectedly compromise the mission's ability to perceive the Universe.

Data availability statement

The data that support the findings of this study are openly available at the following URL/DOI: <https://zenodo.org/records/6954044>; <https://zenodo.org/records/6955182>.

Acknowledgment

Thank you to the Institute for Computing in Research: Mark Galassi and Rhonda Crespo. The authors recognize I Thorpe and J Slutsky at the NASA Goddard Space Flight Center for their data and helpful comments. Additionally, they thank B M Frank, B Piotrkowski, B Bolen, M Cavagliá and S L Larson for their methods and insightful comments. C N Arge, S I Jones-Mecholsky, C J Henney and H Godinez-Vasquez provided key background on space weather. Finally, we thank the anonymous referees for their helpful comments, including elucidating a mistake in the spacecraft coordinate axes. Indie Desiderio-Sloane and Arnold Yang were supported by the Institute for Computing in Research. GDM was supported by multiple Los Alamos National Laboratory internal funding sources, including the Intelligence and Space Research Early Career (ISR-EC) 2022 Pitch Day award XB4F00 and the Center for Space and Earth Science project development award W88600. This document has Los Alamos Unlimited Release (LA-UR) number LA-UR-23-30801. This work was supported by the U.S. Department of Energy through the Los Alamos National Laboratory. Los Alamos National Laboratory is operated by Triad National Security, LLC, for the National Nuclear Security Administration of U.S. Department of Energy (Contract No. 89233218CNA000001).

Supplementary data

The source code and procedures to run it are saved at <https://codeberg.org/Poarthan/solarWindDataAnalysisCode>. LPF data hosted on *Zenodo* was originally supplied by correspondence with I. Thorpe, NASA Goddard Space Flight Center.

ORCID iDs

Arnold Tianyi Yang  <https://orcid.org/0009-0000-3916-1061>

Indie Desiderio-Sloane  <https://orcid.org/0009-0009-1912-7670>

Grant David Meadors  <https://orcid.org/0000-0001-7718-0407>

References

- [1] Amaro-Seoane P *et al* 2017 Laser Interferometer Space Antenna (arXiv:1702.00786)
- [2] Aasi J *et al* 2015 Advanced LIGO *Class. Quantum Grav.* **32** 074001
- [3] Acernese F *et al* 2014 Advanced Virgo: a second-generation interferometric gravitational wave detector *Class. Quantum Grav.* **32** 024001

- [4] Aso Y, Michimura Y, Somiya K, Ando M, Miyakawa O, Sekiguchi T, Tatsumi D, Yamamoto H and Collaboration K 2013 Interferometer design of the KAGRA gravitational wave detector *Phys. Rev. D* **88** 043007
- [5] Lück H et al 1997 The GEO600 project *Class. Quantum Grav.* **14** 1471
- [6] Willke B et al 2002 The GEO 600 gravitational wave detector *Class. Quantum Grav.* **19** 1377
- [7] Abbott B P et al 2016 Observation of gravitational waves from a binary black hole merger *Phys. Rev. Lett.* **116** 061102
- [8] Abbott B P et al 2017 GW170817: observation of gravitational waves from a binary neutron star inspiral *Phys. Rev. Lett.* **119** 161101
- [9] Armano M et al 2016 Sub-femto-g free fall for space-based gravitational wave observatories: LISA Pathfinder results *Phys. Rev. Lett.* **116** 231101
- [10] Armano M et al 2018 Beyond the required LISA free-fall performance: new LISA Pathfinder results down to 20μ Hz *Phys. Rev. Lett.* **120** 061101
- [11] Shaul D et al 2006 Solar and cosmic ray physics and the space environment: studies for and with LISA *AIP Conf. Proc.* **873** 172–8
- [12] Thorpe J I et al 2019 Micrometeoroid events in LISA Pathfinder *Astrophys. J.* **883** 53
- [13] Grimani C and Fabi M 2006 Cosmic-ray and SEP physics with the LISA missions *Proc. 20th European Cosmic Ray Symp. (Lisbon) Portugal*
- [14] Smetana A 2020 Background for gravitational wave signal at LISA from refractive index of solar wind plasma *Mon. Not. R. Astron. Soc.* **499** L77–L81
- [15] Jennrich O, Luetzgendorf N, Thorpe J I, Slutsky J and Cutler C 2021 Sensitivity limits of space-based interferometric gravitational wave observatories from the solar wind *Phys. Rev. D* **104** 062003
- [16] Corbin V and Cornish N J 2006 Detecting the cosmic gravitational wave background with the Big Bang Observer *Class. Quantum Grav.* **23** 2435
- [17] Cutler C and Harms J 2006 Big Bang Observer and the neutron-star-binary subtraction problem *Phys. Rev. D* **73** 042001
- [18] Harry G M, Fritschel P, Shaddock D A, Folkner W and Phinney E S 2006 Laser interferometry for the Big Bang Observer *Class. Quantum Grav.* **23** 4887
- [19] Kawamura S et al 2008 The Japanese space gravitational wave antenna-DECIGO *J. Phys.: Conf. Ser.* **122** 012006
- [20] Kawamura S et al 2011 The Japanese space gravitational wave antenna: DECIGO *Class. Quantum Grav.* **28** 094011
- [21] Abe M et al 2021 Matter-wave Atomic Gradiometer Interferometric Sensor (MAGIS-100) *Quantum Sci. Technol.* **6** 044003
- [22] Frank B M, Piotrkowski B, Bolen B, Cavaglià M and Larson S L 2020 Modeling spurious forces on the LISA spacecraft across a full solar cycle *Class. Quantum Grav.* **37** 175007
- [23] Andersen B N 1991 Virgo-solar irradiance and radiance monitoring on SOHO *Adv. Space Res.* **11** 93–102
- [24] Domingo V, Fleck B and Poland A I 1995 The SOHO mission: an overview *Sol. Phys.* **162** 1–37
- [25] Domingo V and Poland A 1988 SOHO: an observatory to study the solar interior and the solar atmosphere *ESA, The SOHO Mission. Scientific and Technical Aspects of the Instruments*
- [26] Grimani C et al 2006 SEP flux mapping with PHOEBUS *J. Phys.: Conf. Ser.* **32** 6
- [27] Kumar P, White S, Stovall K, Dowell J and Taylor G 2022 Pulsar observations at low frequencies: applications to pulsar timing and solar wind models *Mon. Not. R. Astron. Soc.* **511** 3937–50
- [28] Kaiser M, Kucera T, Davila J, Cyr O C, Guhathakurta M and Christian E 2008 The STEREO Mission: an introduction *Space Sci. Rev.* **136** 5–16
- [29] Ogilvie K et al 1995 SWE, a comprehensive plasma instrument for the wind spacecraft *Space Sci. Rev.* **71** 55–77
- [30] NASA DSCOVR website 2024 (available at: <https://science.nasa.gov/mission/dscovr>)
- [31] Wenzel K-P, Marsden R, Page D and Smith E 1989 Ulysses: The first high-latitude heliospheric mission *Adv. Space Res.* **9** 25–29
- [32] Venzmer M and Bothmer V 2018 Solar-wind predictions for the Parker Solar Probe orbit-near-Sun extrapolations derived from an empirical solar-wind model based on Helios and OMNI observations *Astron. Astrophys.* **611** A36
- [33] Kinnison J, Vaughan R, Hill P, Raouafi N, Guo Y and Pinkine N 2020 Parker Solar Probe: A mission to touch the Sun *2020 IEEE Aerospace Conf. (IEEE)* pp 1–14
- [34] Müller D et al 2020 The Solar Orbiter mission-science overview *Astron. Astrophys.* **642** A1

- [35] MacNeice P 2009 Validation of community models: 2. development of a baseline using the Wang-Sheeley-Arge model *Space Weather* **7** 12
- [36] Lee C, Luhmann J, Odstrcil D, MacNeice P, de Pater I, Riley P and Arge C 2009 The solar wind at 1 AU during the declining phase of solar cycle 23: Comparison of 3D numerical model results with observations *Sol. Phys.* **254** 155–83
- [37] Fichter W, Gath P, Vitale S and Bortoluzzi D 2005 LISA Pathfinder drag-free control and system implications *Class. Quantum Grav.* **22** S139
- [38] Vidano S, Novara C, Colangelo L and Grzymisch J 2020 The LISA DFACS: a nonlinear model for the spacecraft dynamics *Aerosp. Sci. Technol.* **107** 106313
- [39] Navarro-Tapia D and Marcos A 2023 Legacy-based design of the LISA mission science control mode 2023 *IEEE Conf. on Control Technology and Applications (CCTA)* (IEEE) pp 412–7
- [40] Viridis M *et al* 2021 The LISA DFACS: effects of micrometeoroid impacts in the drag-free mode *Int. Astronautical Congress: IAC Proc.* (International Astronautical Federation)
- [41] Schleicher A, Ziegler T, Schubert R, Brandt N, Bergner P, Johann U, Fichter W and Grzymisch J 2018 In-orbit performance of the LISA Pathfinder drag-free and attitude control system *CEAS Space J.* **10** 471–85
- [42] Arge C N and Pizzo V J 2000 Improvement in the prediction of solar wind conditions using near-real time solar magnetic field updates *J. Geophys. Res.* **105** 10465–79
- [43] ACE SWEPAM level 2 data 2016 (available at: https://izw1.caltech.edu/ACE/ASC/level2/lvl2DATA_SWEPAM.html)
- [44] Stone E C, Frandsen A, Mewaldt R, Christian E, Margolies D, Ormes J and Snow F 1998 The advanced composition explorer *Space Sci. Rev.* **86** 1–22
- [45] Nikias C and Mendel J 1993 Signal processing with higher-order spectra *IEEE Signal Process. Mag.* **10** 10–37
- [46] Yang A, Desiderio-Sloane I and Meadors G D 2022 LPF Calibrated Force Data *Zenodo* (<https://doi.org/10.5281/zenodo.6954043>)
- [47] Yang A, Desiderio-Sloane I and Meadors G D 2022 2016 ACE SWEPAM Data Permalink *Zenodo* (<https://doi.org/10.5281/zenodo.6955181>)
- [48] Giulicchi L, Wu S-F and Fenal T 2013 Attitude and orbit control systems for the LISA Pathfinder mission *Aerosp. Sci. Technol.* **24** 283–94
- [49] Hapgood M 1992 Space physics coordinate transformations: a user guide *Planet. Space Sci.* **40** 711–7
- [50] Harris C R *et al* 2020 Array programming with NumPy *Nature* **585** 357–62
- [51] Harris F J 1978 On the use of windows for harmonic analysis with the discrete Fourier transform *Proc. IEEE* **66** 51–83
- [52] Thorpe J, Parvini C and Trigo-Rodríguez J 2015 Detection and measurement of micrometeoroids with LISA Pathfinder *Astron. Astrophys.* **586** 12
- [53] Virtanen P *et al* 2020 SciPy 1.0: fundamental algorithms for scientific computing in Python *Nat. Methods* **17** 261–72
- [54] Tanenbaum A S, Wilcox J M, Franzier E N and Howard R 1969 Solar velocity fields: 5-min oscillations and supergranulation *Sol. Phys.* **9** 328–42